Perception-Aware Tag Placement Planning for Robust Localization of UAVs in Indoor Construction Environments

Navid Kayhani, S.M.ASCE[1]; Angela Schoellig[2]; and Brenda McCabe, M.ASCE[3]

Abstract: Tag-based visual-inertial localization is a lightweight method for enabling autonomous data collection missions of low-cost unmanned aerial vehicles (UAVs) in indoor construction environments. However, finding the optimal tag configuration (i.e., number, size, and location) on dynamic construction sites remains challenging. This work proposes a perception-aware genetic algorithm-based tag placement planner (PGA-TaPP) to determine the optimal tag configuration using four-dimensional (4D) building information models (BIM), considering the project progress, safety requirements, and UAV's localizability. The proposed method provides a 4D plan for tag placement by maximizing the localizability in user-specified regions of interest (ROIs) while limiting the installation costs. Localizability is quantified using the Fisher information matrix (FIM) and encapsulated in navigable grids. The experimental results show the effectiveness of our method in finding an optimal 4D tag placement plan for the robust localization of UAVs on under-construction indoor sites. **DOI: 10.1061/JCCEE5.CPENG-5068.** *© 2022 American Society of Civil Engineers.*

Introduction

Autonomous mobile robots, including unmanned aerial vehicles (UAVs), are regarded as next-generation reality-capture technology for construction applications (Cai et al. 2019). When equipped with cameras, these platforms allow for the automated capture of high-quality images from user-specified locations and angles, which can significantly enhance the performance of downstream vision-based analytics (Hamledari et al. 2017). Robust localization is the first and foremost necessity to enable reliable autonomous navigation (Cadena et al. 2016). Localization is the problem of estimating a mobile system's pose (i.e., position and orientation) with respect to a reference frame. Robustness in localization refers to the method's ability to tolerate perturbations and challenging conditions while preserving the stability and integrity of the estimation. Thus, robust localization entails actively considering perception requirements and environmental information (Yi et al. 2019).

Robotic reality capture solutions deployed on outdoor sites rely mainly on Global Navigation Satellite System (GNSS) signals for localization in autonomous mode (Martinez et al. 2021). In GNSS-denied indoor construction environments, most state-of-the-art autonomous platforms (Asadi et al. 2020; Ibrahim et al. 2019; Xu et al. 2019) rely on environment maps generated in advance by teleoperating the platform within the workspace. However, the layout changes with construction progress, requiring frequent costly and tedious mapping sessions. Additionally, common characteristics of indoor construction settings, such as untextured or repetitive areas (Xu et al. 2020), dynamic or temporary objects (Cadena et al. 2016), and reflective surfaces reduce the quality of prebuilt maps. This approach increases the likelihood of localization failure in indoor construction applications and reduces the system's robustness. Furthermore, the costs of the proposed custom-built prototypes (Asadi et al. 2020; Kim et al. 2018) and commercial products limit their scalability and applicability in practice.

To reduce the cost of automated indoor data collection and address the technical challenges discussed, Kayhani et al. (2022) previously proposed a low-cost, lightweight, versatile, tag-based visual-inertial localization method using AprilTags. Even though the tags themselves have almost no cost, the manual tag installation process might become a tedious task if improperly planned (Kayhani et al. 2020). With changes in the interior layout, some tags may be occluded or need replacement, the target areas to be monitored or no-fly zones may vary, and tag placement options may change. Larger tags can be detected from longer ranges, whereas printing them on standard-sized sheets (e.g., letter or A4) may be more convenient and less costly. The number of tags must be kept at a minimum to limit the amount of manual work for placing and maintaining tags. Finally, the opted tag number, size, and location must result in robust and high-quality tag-based visual-inertial localization. These considerations highlight that experience-based tag placement planning is nontrivial and time-demanding, and may result in performance deviations.

The question arises about optimizing the tag placement/replacement process on an indoor construction site by maximizing localizability with a limited number of tags considering construction progress, project schedule, and safety requirements. Localizability, herein, refers to the agent's ability to reliably locate itself with low uncertainty and represents the estimation quality and robustness. This work addressed the problem of 4D tag placement, which aims to find the optimal tag configuration (i.e., number, size, and location) over time, considering the construction schedule and safety constraints (e.g., no-fly zones). The optimal solution maximizes the tag-based visual-inertial localization quality and certainty (i.e., tag-based localizability) while minimizing installation costs. The pose estimation certainty can be quantified using the Fisher information (Zhang and Scaramuzza 2019). Therefore, the maximum tag-based localizability is achieved by devising a tag

[1]Ph.D. Candidate, Dept. of Civil and Mineral Engineering, Univ. of Toronto, Toronto, ON, Canada M4S A4 (corresponding author). ORCID: https://orcid.org/0000-0001-8139-7254. Email: navid.kayhani@mail.utoronto.ca

[2]Associate Professor, Institute for Aerospace Studies, Univ. of Toronto, North York, ON, Canada M3H 5T6.

[3]Professor, Dept. of Civil and Mineral Engineering, Univ. of Toronto, Toronto, ON, Canada M4S 1A4.

Note. This manuscript was submitted on June 28, 2022; approved on October 1, 2022; published online on December 21, 2022. Discussion period open until May 21, 2023; separate discussions must be submitted for individual papers. This paper is part of the ***Journal of Computing in Civil Engineering***, © ASCE, ISSN 0887-3801.

configuration with the highest expected information gained from tag measurements. Minimizing the installation costs is obtained by limiting the number of tag placements, replacements, and removals during the project.

Tag placement planning can be viewed as a constrained combinatorial optimization problem. It maximizes a localizability utility function within user-specified regions of interest (ROIs) while minimizing a cost function to penalize tag network modifications. ROIs include onsite target work zones and travel paths connecting these target locations with different importance levels. The utility function represents the likelihood of getting high-quality tag measurements by evaluating the attainable photometric information at each query point within ROIs. In other words, utility is determined not only by the tags' visibility but also by their informativeness. Minimizing the number of tag placements, replacements, and removals is obtained by associating a negative utility (i.e., cost) for adding, substituting, or removing tags in the network.

This study addresses the gap in the literature by proposing a 4D building information model (BIM)-based solution for the automated design of tag placement plans, considering indoor construction dynamics. A perception-aware genetic algorithm-based tag placement planner (PGA-TaPP) is proposed to find the optimal tag configuration. It maximizes localizability while minimizing the total cost of tag installations by incorporating the project schedule and safety requirements. PGA-TaPP considers multiple project phases, tag placement heights, flight altitudes, and localizability metric functions. The proposed method inputs the project's 4D BIM, ROIs, no-fly zones, and user-specified design parameters. Each project comprises construction phases, representing project snapshots at different times. The site layout geometry of every phase is automatically extracted. Each phase is horizontally sliced to generate 2D scenes corresponding to different flight altitudes. Scenes, made up of polygons and ROIs, are further quantized to obtain discrete tag placement options and UAV query poses. The gainable information from query poses in the workspace is quantified using the Fisher information matrix (FIM). Finally, the developed genetic algorithm engine optimizes the tag configuration throughout the entire project such that (1) the overall tag-based localizability within ROIs is maximized; (2) the tag configuration adjustments are minimal; and (3) safety requirements are satisfied. The main contributions of this work are (1) proposal of a perception-aware 4D tag placement planning method to find the optimal tag number, size, and location for supporting robust tag-based visual-inertial localization on indoor sites considering localizability, project schedule, installation costs, and safety; (2) quantification of attainable information for 6-DoF tag-based visual-inertial localization using Fisher information with various metric functions; and (3) quantitative evaluation of the performance of the proposed tag networks in a BIM-enabled simulation environment.

Background

Automated Data Collection Using Mobile Robots

Frequent, reliable, and high-quality data from the job site are necessary for a systematic performance evaluation of architecture, engineering, and construction (AEC) projects (Moselhi et al. 2020). With advances in computer vision-based solutions, RGB images are considered one of the most valuable data modalities for automating inspection and monitoring tasks (Pal and Hsieh 2021). However, manual visual data acquisition is time-consuming, error-prone, and costly (Teizer 2015). In the past decade, automated data collection using autonomous mobile robots has gained momentum in the AEC community. Previous studies have extensively reviewed these applications (Cai et al. 2019; Ham et al. 2016; Rakha and Gorodetsky 2018). Outdoor visual data collection for infrastructure inspection (Freimuth and König 2018; Lin et al. 2021), earthwork surveying (Siebert and Teizer 2014), quality control (Kielhauser et al. 2020), safety inspection (Gheisari et al. 2014; Martinez et al. 2021), as well as indoor progress monitoring (Hamledari et al. 2017) are some examples of the extensive use of UAVs in construction applications. However, UAVs in these studies were remotely controlled or relied on GNSS signals for autonomous flight. Autonomous ground robots were also deployed indoors for environmental air quality (Jin et al. 2018), construction progress monitoring (Asadi et al. 2020), semantic modeling (Adán et al. 2020), and building retrofit performance simulation (Mantha et al. 2018). Table 1 provides some examples of the applications of mobile robots in automated data collection in the AEC industry.

Indoor Localization in Construction Settings

Indoor construction sites are unique GNSS-denied environments. These settings present technical difficulties for many localization methods. Wave-based methods such as wireless local area networks (WLAN) (Deasy and Scanlon 2004), radio-frequency identification (RFID) (Liu et al. 2014; Razavi and Moselhi 2012), and ultra-wideband (UWB) (Witrisal and Meissner 2012) lose their accuracy and are unreliable in indoor construction settings due to interference with construction materials (e.g., steel) (Ibrahim and Moselhi 2016). A common technique for navigating unknown workspaces is to concurrently map the environment and localize the agent within the built map, referred to as simultaneous localization and mapping (SLAM). Modern SLAM architectures constitute a back-end state estimation component supported by a sensor-dependent front end for feature extraction, data association, and loop closure (i.e., recognizing a previously observed place) (Cadena et al. 2016). Loop closure is necessary to reset the localization error and estimate the actual topology of the environment in the map. SLAM reduces to odometry without loop closure, which drifts over time and is unreliable for long-term navigation.

Table 1. Automated data collection using mobile robots

Application areas	Platform	Localization	Indoors	Application examples
Infrastructure inspection	Aerial	GNSS	No	Freimuth and König (2018)
Bridge inspection	Aerial	GNSS	No	Lin et al. (2021)
Earthwork surveying	Aerial	GNSS	No	Siebert and Teizer (2014)
Quality control	Aerial	GNSS	No	Kielhauser et al. (2020)
Safety inspection	Aerial	GNSS	No	Martinez et al. (2021)
Progress monitoring	Aerial + ground	Prebuilt maps	Yes	Asadi et al. (2020)
Environmental air quality	Ground	Prebuilt maps	Yes	Jin et al. (2018)
Semantic modeling	Ground	Prebuilt maps	Yes	Adán et al. (2020)
Building retrofit performance	Ground	AprilTags	Yes	Mantha et al. (2018)

In recent decades, significant research has been conducted to improve localization and state estimation accuracy and efficiency in GNSS-denied environments, with promising outcomes (Delmerico and Scaramuzza 2018). However, these results have been demonstrated only for particular domains and given a hardware-environment-performance combination (Cadena et al. 2016). For instance, successful SLAM/mapping missions with sufficient accuracy (<10 cm) in an office building involving a ground robot with wheel encoders, a laser scanner, and enough computational and power resources are achievable (Mur-Artal et al. 2015). However, performing SLAM/mapping may fail in highly dynamic environments with perceptual aliasing and feature scarcity (Cadena et al. 2016), and is considered resource-intensive for large environments (Muñoz-Salinas et al. 2019).

Tag-Based Visual-Inertial Localization

Fiducial markers such as AprilTags (Wang and Olson 2016) are planar artificial landmarks consisting of patterns. They provide robust data association and are ideal for featureless or repetitive areas common in construction settings. Tags are often employed for local positioning tasks such as map initialization and UAV landing (Brommer et al. 2018). For long-term localization, visual-SLAM based on only tags (Muñoz-Salinas et al. 2019) and coupled with keypoints (Muñoz-Salinas and Medina-Carnicer 2020) were proposed. Relying only on vision reduces their reliability in the face of occlusion or motion blur. Tag-based visual-inertial localization (Kayhani et al. 2022) is an inexpensive alternative to enable autonomy for low-cost UAVs to be deployed for automated data collection in indoor construction settings. This method uses tags with known sizes and locations, jointly acting as a quasi-map of the environment. A 3D position accuracy as low as 2–5 cm was obtained in the experiments conducted in the laboratory and simulation settings. Our proposed formulation is based on an on-manifold extended Kalman filter (EKF), suitably addressing the topological structure of the rotation and pose groups in 3D. It integrates two sources of information to yield consistent 6-DoF global pose estimates in real-time: (1) odometry-based rotational and translational velocities; and (2) tag-based visual measurements

$$\text{Motion model } \mathbf{x}_k = f(\mathbf{x}_{k-1}, \mathbf{u}_{k-1}) + \mathbf{w}_{k-1} \tag{1}$$

$$\text{Measurement model } \mathbf{y}_k = g(\mathbf{x}_k) + \mathbf{n}_k \tag{2}$$

An EKF involves two steps as a recursive filter: prediction and correction. The prediction step propagates the current state mean and covariance estimates forward in time. The current pose $\mathbf{x}_k$ is predicted based on the previous pose estimate $\mathbf{x}_{k-1}$ and the odometry-based velocities (inputs) $\mathbf{u}_{k-1}$ considering a zero-mean Gaussian noise $\mathbf{w}_{k-1}$ through a motion model $(f(\cdot))$ [see Eq. (1)]. The predictions are updated in a correction step in which tag measurements $\mathbf{y}_k$ are incorporated, and the posterior mean and covariance are estimated. The correction is based on a measurement model $(g(\cdot))$, perturbed by a zero-mean Gaussian noise $(\mathbf{n}_k)$ [Eq. (2)]. In a related study (Neunert et al. 2016), a tag-based visual-inertial EKF-SLAM was proposed. However, the proposed filter-based SLAM can only map a limited number of tags in real-time, limiting its application on large construction sites.

Tag-Based Localization Quality and Fisher Information

Considering the reliability of autonomous navigation at the planning stage prioritizes tag configurations that can result in high-quality localization. The observed tag's information must be quantified to incorporate the knowledge about tag-based visual-inertial localization quality. Fisher information is often used to represent this knowledge (Zhang and Scaramuzza 2019). According to the Cramér-Rao lower bound (CRLB), the covariance of any unbiased estimate $\mathbf{x}$, given a set of measurements $\mathbf{y}$, is bounded by the inverse of the FIM (Barfoot 2017), denoted as $\mathbf{I}_\mathbf{x}(\mathbf{y})$. In other words, the measurement information about the parameter to be estimated establishes a fundamental limit on how confident the estimates can be, regardless of the form of the estimator, and the FIM quantifies this notion. Because localization is essentially a pose estimation problem, the FIM can be applied to quantify the estimation uncertainty and, therefore, viewed as a metric for localization quality quantification.

Given that the measurement process of the state (i.e., 6-DoF UAV's pose) can be described as a likelihood function $p(\mathbf{y}|\mathbf{x})$, the observed Fisher information can be defined as (Barfoot 2017):

$$\mathbf{I}_\mathbf{x}(\mathbf{y}) = E\left[\left(\frac{\partial \ln p(\mathbf{y}|\mathbf{x})}{\partial \mathbf{x}}\right)^T \left(\frac{\partial \ln p(\mathbf{y}|\mathbf{x})}{\partial \mathbf{x}}\right)\right] \tag{3}$$

Assuming zero-mean Gaussian noise with constant covariance $\mathcal{N}(\mathbf{0}, \mathbf{\Sigma})$ for measurements, Eq. (3) can be rewritten as (Wang and Dissanayake 2008):

$$\mathbf{I}_\mathbf{x}(\mathbf{y}) = (\mathbf{G}_\mathrm{x})^\mathrm{T} \mathbf{\Sigma}^{-1} \mathbf{G}_\mathrm{x} \tag{4}$$

where $\mathbf{G}_\mathrm{x}$ = Jacobian of the measurement model in Eq. (2)

$$\mathbf{G}_\mathbf{x} = \frac{\partial g}{\partial \mathbf{x}} \tag{5}$$

Methods

Overview

In this work, 4D-BIM is utilized to retrieve the project's spatial-temporal information and incorporate the dynamic nature of indoor construction environments. As illustrated in Fig. 1, the proposed method inputs the project 4D-BIM in Autodesk Revit (Autodesk, Inc., San Rafael, California) or Industry Foundation Classes (IFC) format to address the ease of design and facilitate interoperability. The 4D-BIM includes the 3D model, project schedule, and ROIs for the time-stamped construction phases. Other inputs include the UAV's camera specifications, tag information, and design factors such as planning and optimization parameters.

The Initialization and Geometry Extraction module automatically extracts the type, geometry, positioning, and relationship of the relevant elements for each time-stamped construction phase, converts them to a set of 2D polygons, and stores them as separate files. These files are then fed into the proposed PGA-TaPP to find the optimal tag configuration that supports robust tag-based visual-inertial localization, considering the project progress and schedule. The extracted geometry of the site layout, ROIs for each phase, and input parameters are fed to the Modeling and Problem Formulation module. These parameters include the UAV's camera specifications [e.g., depth of view (DoV), lens parameters, and vehicle-to-camera transform], tag information (e.g., available sizes, installation heights, maximum number), and planning parameters (e.g., flight altitudes, discretization resolutions, and no-fly zones). A set of 2D scenes corresponding to each flight altitude is first generated, each of which comprises polygons representing modified ROIs and building elements. The polygons are further quantized to obtain grids, (i.e., discretized navigable areas) and tag placement locations. The discretized navigable areas constitute constraint-free grid cells

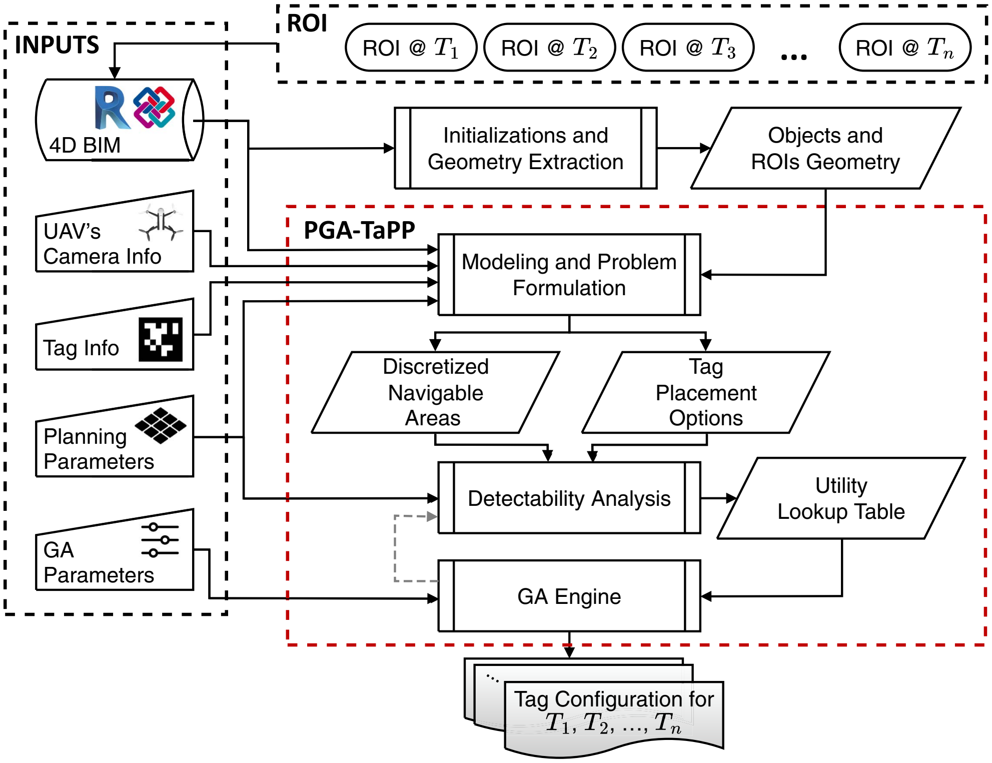

Fig. 1. Overview of proposed method.

within ROIs at each flight altitude. Tag placement options are a discrete set of feasible tag installation locations in each phase.

To calculate the utility function for a solution (i.e., tag placement network) in a particular time-stamped construction phase, PGA-TaPP quantifies the quality of expected tag measurements in discretized UAV orientations within every ROI cell. It first identifies the tags visible from each pose and assigns a utility to the given query pose. The utility of the query pose is calculated separately for each visible tag and is a function of the FIM (more discussion can be found in the section "Scoring Metric Functions for Localizability Evaluation"). A lookup table is then constructed to efficiently search the solution space based on the identified discretized navigable areas, the tag placement options, and the planning parameters. The created lookup table allows for efficient querying of the utility for any UAV pose and tag placement option. The table can be constructed entirely prior to GA-based optimization or as the optimization process is performed. In the former mode, the Detectability Analysis module extensively explores the tag placement possibilities for efficient exploitation in searching the solution space by the optimization module, denoted as GA Engine. Finally, the GA Engine finds the tag configuration for each construction phase by maximizing the vehicle's localizability with minimal tag configuration modifications throughout the project. The resulting tag configuration for each time-stamped construction phase is visualized for enhanced communication.

Initializations and Geometry Extraction

The Initializations and Geometry Extraction module takes the project's 4D-BIM model as input. This module uses an application programming interface (API) to handle Revit files and relies on open-source libraries to read IFC files in the back end. Supporting both formats is essential because IFC is a neutral schema that allows interoperability (Laakso 2012), yet is arguably more suitable for information retrieval than design. In contrast, users may need to modify the planning constraints (e.g., ROIs or no-fly zones) or incorporate potential discrepancies between BIM and the actual site conditions throughout the project. The discrepancies can be caused by modeling errors, infrequent 4D-BIM updating, or temporary site objects. These changes can be made more conveniently in a modeling tool with a graphical user interface such as Autodesk Revit.

The project is first divided into time-stamped construction phases (i.e., $T_1, T_2, \ldots, T_{\mathrm{m}}$) according to a given data collection mission plan. The algorithm checks if the BIM file has a Project Base Point to set the origin of the global coordinate system. If no base point is found, an arbitrary but consistent base point is chosen, for example, the bottom left corner of the building envelope. For each construction phase, for example, T_i ($i \in [1, 2, \ldots, \mathrm{m}]$), it automatically selects the relevant building elements (e.g., walls, partitions, doors, windows, columns), ROIs, and no-fly zones. The indoor site layout at T_i is further divided into discretized altitudinal layers to account for the UAVs' 3D maneuver and its impact on camera field of view (FoV) and tag detectability (Fig. 2). The navigable altitude of the UAV might also change with construction progress. For example, installing suspended ceilings or electrical fixtures reduces the maximum safe flight altitude (Hamledari et al. 2021). Thus, the unnavigable areas at each altitudinal layer are added to no-fly zones at the corresponding altitude. Finally, the indoor site layout at each layer is reduced to a set of 2D polygons, including building elements, ROIs, and no-fly zones.

Perception-Aware Genetic Algorithm-Based Tag Placement Planner

PGA-TaPP involves four main steps: (1) camera and scene modeling; (2) optimization formulation and localizability metric establishment; (3) detectability analysis and utility calculations: and (4) GA-based optimization. The first two steps are included in

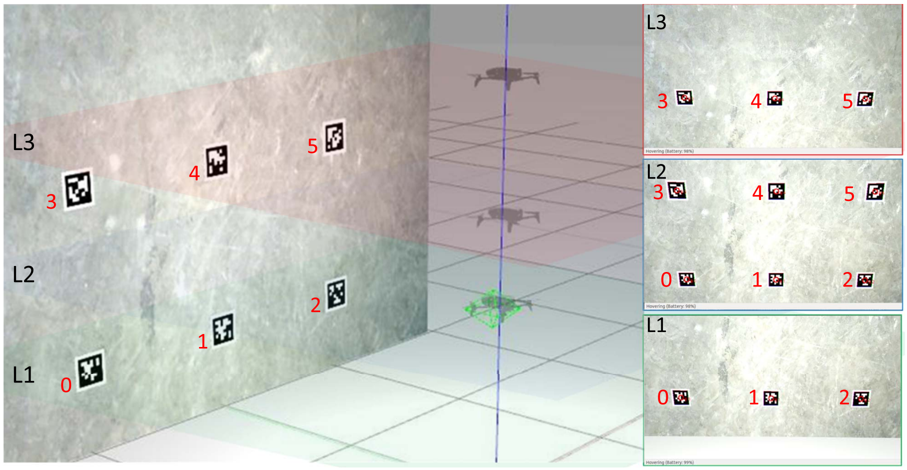

Fig. 2. Altitudinal layers and detected tags in the image stream captured at each flight altitude.

the Modeling and Problem Formulation module, and Detectability Analysis and GA Engine handle the rest.

Modeling and Problem Formulation

UAV specifications, tag information, planning parameters, and the extracted geometric information from building elements, ROIs, and no-fly zones are fed to the first module in PGA-TaPP for scene modeling and problem formulation. This section discusses the module's components: camera and measurement models, scene modeling, and scoring metric formulation.

Camera and Measurement Models. The UAV's camera is represented as a pinhole camera model with given intrinsics (e.g., optical center, focal length, and field of view) and the camera-to-vehicle transformation. This allows for covering different robotic platforms with arbitrary camera configurations. Without loss of generality, it is assumed that the UAV has only one camera on board for the rest of this discussion. The 3D coordinates of the nth corner point (e.g., $n \in \{1,2,3,4\}$ for square markers) of tag j expressed in the camera frame, $\mathbf{p}_c^{p_{\tau_j,n}c}$, can be written as (Kayhani et al. 2022):

$$z^{\tau_j,n}(\mathbf{x}) = \mathbf{p}_c^{p_{\tau_j,n}c} = \mathbf{D}^T\mathbf{T}_{cv}\mathbf{T}_{vw}\mathbf{p}^w_{\tau_j,n} = [X \quad Y \quad Z]^T \qquad (6)$$

where $\mathbf{p}^w_{\tau_j,n}$ = homogenous coordinate of the nth corner point of tag j in the world frame; and $\mathbf{T}_{vw} = \{\mathbf{r}_w^{vw}, \mathbf{C}_{vw}\} \in SE(3)$ = vehicle's pose expressed in the world frame and the state to be estimated $(\mathbf{x})$. Additionally, $\mathbf{T}_{cv}$ is the vehicle-to-camera transformation known from calibration, and $\mathbf{D}^T = [\mathbf{1}_3|\mathbf{0}_{3\times 1}]$ is a dilated identity matrix to refine the matrix dimensions.

Denoting the pinhole camera model that projects $\mathbf{p}_c^{p_{\tau_j,n}c}$ into a rectified image as $s(\cdot)$, the measurements (i.e., the pixel coordinates of the nth corner point of tag j) are obtained as (Kayhani et al. 2022):

$$g^{\tau_j,n}(\mathbf{x}) = s(z^{\tau_j,n}(\mathbf{x})) = \begin{bmatrix} u \\ v \end{bmatrix} = \mathbf{D_p}\begin{bmatrix} f_u & 0 & c_u \\ 0 & f_v & c_v \\ 0 & 0 & 1 \end{bmatrix}\frac{1}{Z}\begin{bmatrix} X \\ Y \\ Z \end{bmatrix} \qquad (7)$$

where $g^{\tau_j,n}(\mathbf{x})$ = noise-free measurement model; c_u and c_v = optical offsets (principal point); f_u and f_v = camera focal lengths; and $\mathbf{D_p} = [\mathbf{1}_2|\mathbf{0}_{2\times 1}]$ = dilated identity matrix.

Before localizability quantification for a pose, it is essential to identify the tags detectable in the image captured by the vehicle at that query pose. A tag can be detected from $\mathbf{T}_{vw}$ if (1) it can be observed from the vehicle position $\mathbf{r}_w^{vw}$, considering occlusions; and (2) it is within the camera FoV. The former is obtained using visibility analysis and generating a visibility graph (Lozano-Pérez and Wesley 1979) to identify visible tag corners $(\mathbf{P}^{\tau_j w})$. The latter is achieved by projecting the tag corners onto image plane [Eq. (7)] and checking whether the projected pixel coordinates $\boldsymbol{\pi} = [u, v]^T$ are within the image boundary I [Eq. (8)]. More details are provided in the "Detectability Analysis" section

$$v(\mathbf{T}_{vw}, \mathbf{P}^{\tau_j w}) = \begin{cases} 1, & \boldsymbol{\pi} \in I \\ 0, & \boldsymbol{\pi} \notin I \end{cases} \qquad (8)$$

Scene Modeling. As shown in Fig. 3, a project is divided into phases, corresponding to snapshots of the project. Accounting for the 3D maneuver of UAVs, each phase is subdivided into altitudinal layers (Fig. 2), considering the safety of operation. Accordingly, a 2D scene is generated for each altitudinal layer to model the given indoor site at time T_i. Each scene initially consists of 2D polygons representing building elements, ROIs, and no-fly zones. The building elements collectively correspond to inside and outside boundaries, obstacles, and surfaces for tag installation. The ROI polygons specify the geometry within which the localizability must be maximized, whereas no-fly zones represent areas where the UAV is prohibited from operating. The difference between ROI and no-fly zone polygons is found for each scene to find the navigable area, denoted as modified ROIs.

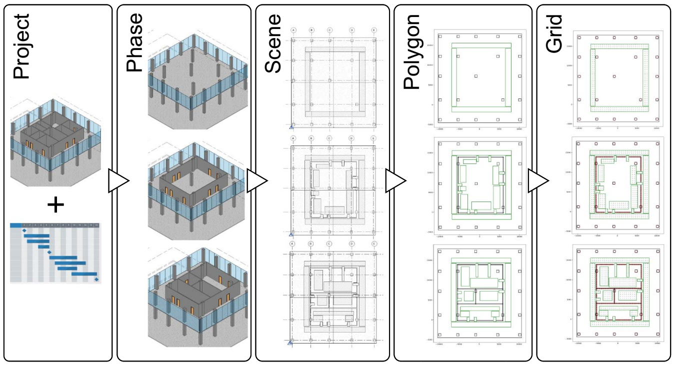

Fig. 3. Hierarchy of spatial objects in PGA-TaPP.

Algorithm 1 Tag Option Identification

```
INPUT $obs$, $d_{res}$, $t_{size}$                              ▷ $obs$: obstacles
RETURN List$[x, y, u, v]$                              ▷ tag direction = $[u, v]$
$dist$ = FindMinimumTagDistance($d_{res}, t_{size}$)
$\epsilon = 5 \times 10^{-5}$
for $poly$ in $obs$ do
    $poly$ = Scale($poly$, $1+\epsilon$)           ▷ to avoid overlaps with surface
    $lines$ = DecomposePoly($poly$)                        ▷ list of surfaces
    for $line$ in $lines$ do
        $x$, $y$ = InterpolateByDistance($line$, $dist$)
        $u$, $v$ = GetNormal($line$)
        List.append($x, y, u, v$)
    end for
end for
return List
```

Fig. 4. Algorithm for identifying quantized tag placement options in 2D.

Modified ROI polygons are then quantized into grid cells. The default grid cell size is set to 0.5×0.5 m, considering compact UAVs' dimensions plus a clearance buffer to guarantee safety. The center of the grid cells constitutes the query points for evaluating localizability. We note that the query point corresponds to the vehicle position, and the camera pose is obtained using the inputted vehicle-to-camera transform ($\mathbf{T}_{cv}$). Our approach finds the optimal tag network from a discrete space of possible tag placement locations. Tag placement options are determined based on user-specified installable surfaces, discretization resolution, and tag size(s) such that tags do not overlap. Considering practicality, economy, and ease of installation, the potential tag placement heights are limited to those at which tags can be installed without extra apparatus and additional labor input. The algorithm for finding quantized tag placement options in 2D is summarized in Fig. 4. The 2D options found are then added to each level to consider multilevel tag placement (Fig. 2).

Fisher Information Matrix for Tag-Based Visual-Inertial Localization. This section focuses on formulating the Fisher information for a single pose in on-manifold tag-based visual-inertial localization. Calculating the FIM [Eq. (4)] for a single pose $\mathbf{x} = \mathbf{T}_{vw}$ requires calculating the Jacobian of the observation of nth corner point of tag j as in Eq. (9). The Jacobian in Eq. (9) is calculated using two factors defined in Eqs. (10) and (11). These factors come from the introduced nonlinearities in the measurement model [Eq. (7)] linearized about their mean [for more details on Jacobian derivations, see (Kayhani et al. 2022)]

$$\mathbf{G}^{\tau_j,n} = \frac{\partial g^{\tau_j,n}(\mathbf{x})}{\partial \mathbf{x}} = \frac{\partial}{\partial \mathbf{x}}(s(z^{\tau_j,n}(\mathbf{x}))) = S^{\tau_j,n} Z^{\tau_j,n} \tag{9}$$

$$S^{\tau_j,n} = \mathbf{D}_p \begin{bmatrix} f_u & 0 & c_u \\ 0 & f_v & c_v \\ 0 & 0 & 1 \end{bmatrix} \begin{bmatrix} \frac{1}{Z} & 0 & -\frac{X}{Z^2} \\ 0 & \frac{1}{Z} & -\frac{Y}{Z^2} \\ 0 & 0 & 0 \end{bmatrix} \tag{10}$$

$$Z^{\tau_j,n} = \mathbf{D}^T \mathbf{T}_{cv} (\mathbf{T}_{vw} \mathbf{p}^{w}_{\tau_j,n})^{\odot} \tag{11}$$

Calculating $Z^{\tau_j,n}$ in Eq. (9) requires introducing $(\cdot)^{\odot}$ operator (Barfoot 2017) that acts on 4×1 points in homogenous coordinates following Eq. (12), where the first three components ($\boldsymbol{\varepsilon} \in \mathbb{R}^3$) are expressed in the skew-symmetric matrix format [Eq. (13)]

$$\mathbf{p}^{\odot} = \begin{bmatrix} sx \\ sy \\ sz \\ s \end{bmatrix}^{\odot} = \begin{bmatrix} \boldsymbol{\varepsilon} \\ \eta \end{bmatrix}^{\odot} = \begin{bmatrix} \eta \mathbf{1} & -\boldsymbol{\varepsilon}^{\wedge} \\ \mathbf{0}^T & \mathbf{0}^T \end{bmatrix} \in \mathbb{R}^{4\times 6} \tag{12}$$

$$\boldsymbol{\varepsilon}^{\wedge} = \begin{bmatrix} \varepsilon_x \\ \varepsilon_y \\ \varepsilon_z \end{bmatrix}^{\wedge} = \begin{bmatrix} 0 & -\varepsilon_z & \varepsilon_y \\ \varepsilon_z & 0 & -\varepsilon_x \\ -\varepsilon_y & \varepsilon_x & 0 \end{bmatrix} \tag{13}$$

The FIM for tag j observed at $\mathbf{T}_{vw}$ is calculated using Eq. (4) and denoted as $\mathbf{I}_{\tau_j}(\mathbf{T}_{vw})$. Let $\mathcal{T} \subset \{\tau_1, \tau_2, \ldots, \tau_M\}$ be the set of all tags detected in the image taken at the same vehicle pose, and we have

$$\text{FIM}(\mathbf{T}_{vw}) = \sum_{\tau_j}^{\tau_j \in \mathcal{T}} \mathbf{I}_{\tau_j}(\mathbf{T}_{vw}) \tag{14}$$

Scoring Metric Functions for Localizability Evaluation. The FIM is incorporated in the proposed optimization formulation to consider localization quality and quantify vehicle localizability. In any GA-based optimization, a mechanism is required to determine the utility (i.e., fitness) of the generated solutions (i.e., population), such that those with higher values survive and others are eliminated (i.e., selection). Therefore, the information matrix is mapped to a single scalar using a nonnegative metric function $\mathcal{M}(\cdot)$. This work incorporates the log-determinant, the trace, and the smallest eigenvalue as metric functions directly obtained from the FIM. Some fundamental properties of these metric functions are briefly reviewed to provide more intuition. The FIM determinant can be a proper information measure because its absolute value geometrically represents the volume of square matrices in n dimensions. The larger the volume, the more informative the measurement will be in the case of the FIM. In this work, the transformed logarithm of the determinant is used to yield more numerical stability. The trace of a matrix is equal to the sum of its eigenvalues, and eigenvalues describe how a linear transformation stretches the space in a particular direction. Maximizing trace, also known as A-optimality, guarantees that the majority of the state space dimensions are considered. In a similar sense, the smallest eigenvalue represents the least affected direction. It corresponds to E-optimality, aiming to improve the worst-case variances of the parameter set by maximizing the smallest eigenvalue of the FIM.

Detectability Analysis

To quantify the expected attainable information from a query pose $\mathbf{P}_q(x_q, y_q, z_q, \theta_q)$, it is essential to predict the detectable tags from that pose. The necessary condition for a tag to be detectable is its visibility from the query pose. For square tags such as AprilTags, it is required to have all four corners in view to guarantee visibility (Kayhani et al. 2020); that is, the corners should be within the camera's FoV and not occluded. Occlusion is found based on the camera line of sight, depending only on the camera and tag position. However, being within FoV depends on the vehicle's pose and camera intrinsics. A minimum side length threshold ($SL_{\min}$) is defined to reliably predict the detectability of tags (Fig. 5). The AprilTag detection algorithm (Wang and Olson 2016) has a preset threshold for rejecting small line segments (i.e., 4 pixels) in its line-fitting module to minimize the chance of false-positive tag detections. It was experimentally observed that the minimum side length of the tag for reliable detections in practice is 15–20 pixels (Kayhani et al. 2019).

```
Algorithm 2 Tag Detectability and FIM Calculation
INPUT $p_q(x, y, z)$, $\mathbf{p}_q(p_q, \theta)$, $scene$, $t_{locID}$    ▷ $t_{locID}$: tag's location ID
RETURN FIM
$UAV = scene$.uav, $Camera = UAV$.camera, $T_{cv} = UAV$.Tcv,
$DoV = Camera$.dov $K = Camera$.k    ▷ $K$: camera intrinsics
FIM = ZEROS(6,6)
$p_c$ = FINDTAGCENTER($t_{locID}$)
$p_1, p_2, p_3, p_4$ = FINDTAGCORNERS($t_{locID}$, $t_{size}$)
if DIS($p_c, p_q$) < $DoV$ then
    for $i$ in $[1, 2, 3, 4]$ do
        if !(LEEVISIBILITY($p_i$, $p_q$), INFOV($p_i$, $\mathbf{p}_q$, $K$)) then
            return FIM
        end if
    end for
    $L_{min}$ = MINPROJECTEDLENGTH($camera, p_1, p_2, p_3, p_4, p_q$)
    if $L_{min} > SL_{min}$ then
        for $i$ in $[1, 2, 3, 4]$ do
            FIM += CALCULATEFIM($T_{cv}, K, p_i, p_q$)    ▷ Eq. 9-13
        end for
    end if
end if
return FIM
```

Fig. 5. Algorithm for tag detectability analysis and FIM calculations for a single UAV pose and tag.

Genetic Alorgithm Engine

Finding the 4D tag configuration that maximizes the localizability with the lowest installation costs, considering indoor site dynamics, is a constrained combinatorial optimization and nondeterministic polynomial-time (NP)–hard problem. A genetic algorithm (GA) is adopted in this work to tackle this optimization problem due to its advantages: (1) it can identify near-optimal solutions; (2) it has a low tendency to get stuck at local optima due to mutation; (3) it could be parallelized for efficient concurrent computations; and (4) it can handle multiobjective fitness functions and flexible policies. The GA-based optimization in PGA-TaPP is handled by an engine, developed with a modular architecture and parallel computation capabilities. The latter is a highly desirable feature in GA-based optimization, because the fitness function calculations are often the bottleneck. The former allows for deploying different fitness functions and GA operators such as selection, mutation, and crossover.

The first requirement for employing GA-based optimization is defining a genetic representation of a feasible solution to the problem (i.e., chromosomes). In this work, chromosomes are structured as a sequence of elements (i.e., genes) representing the collection of all tag placement options in all construction phases (Fig. 6). Each gene is associated with a global identifier, a tag location ID (ij), unique among construction phases. A location ID ij corresponds to tag location i in construction phase T_j, which can point to a feasible or infeasible tag placement option at T_j depending on the site layout. For example, if a wall is built at T_m, then the tag options corresponding to that wall are infeasible for the previous phases. Genes can take any nonnegative integer value between zero and the number of tag sizes ($\tau_{ij} \in [0, n_s]$). Zero corresponds to no tags placed at the corresponding location, while any integer greater than zero embodies the installation of a particular tag size. If only a single tag size is available, the chromosomes will reduce to binary.

To determine the best solution (fittest chromosome) in each iteration (population), a mapping (fitness function) is needed to assign a score (fitness score) to the generated solutions by the GA. The fitness score for a given chromosome is calculated based on a utility (U) that maximizes localizability and a cost (J) that minimizes the installation costs by penalizing changes in the network in and between phases, as follows:

$$\mathrm{Score} = U - J \tag{15}$$

For any given tag configuration, the gridwise utility matrix for $roi \in ROI$ in phase T_i is denoted as $\boldsymbol{U}_{roi}$ and obtained using Eq. (16). This requires estimating the expected FIM for each query cell $c_q(x_q, y_q)$ and mapping the obtained matrix value to a scalar using scoring metric function $\mathcal{M}(\cdot)$. Estimating the FIM for $c_q(x_q, y_q)$ involves determining the FIM (Fig. 5) for all discrete query poses in each scene $s \in S$, corresponding to the altitudinal layer z_q, with discrete yaw angles θ_q quantized by a user-specified rotational step ($\Delta\theta$) (e.g., 5°). By calculating the gridwise utility, the algorithm respects the spatial structure of the grid cells. Finally, the phase U_{T_i} and the total utility U are found by aggregation using Eq. (17), where I_{roi} is a relative importance factor associated with roi

$$\boldsymbol{U}_{roi} = \sum_{z_q}^{s\in S} \sum_{\theta_q}^{\theta_q\in\theta} \mathcal{M}(\mathrm{FIM}(x_q, y_q, z_q, \theta_q)), \quad \forall\ c_q(x_q, y_q) \in roi \tag{16}$$

$$U = \sum_{i=1}^{m} U_{T_i}, \qquad U_{T_i} = \sum_{roi}^{roi\in ROI} I_{roi} \times \mathrm{sum}(\boldsymbol{U}_{roi}) \tag{17}$$

Utility calculations can be coupled or decoupled with the main GA optimization flow. When coupled, the tag placement options are explored as the current chromosome is evaluated (Fig. 7). The FIM for each query pose and tag location ID pair is calculated once in exploration and stored in a hash lookup table for efficient exploitations. The entire tag options in T_i can be exhaustively explored prior to optimization as an alternative. In both cases, parallel processing techniques were used to increase exploration efficiency. However, the decoupled approach allows for normalizing the gridwise utility by the maximum utility obtainable from the grid, enhancing score interpretability and facilitating cost parameter assignments. The maximum utility is obtained when all tag placement options are occupied. Normalizing the gridwise utility brings the utility between zero and one, represents the utilized capacity of each cell, and allows for easier comparisons and interpretability

$$J = w_{plc}\left[\sum_{i=1}^{n_s} \frac{n_{plc_i}}{\alpha_i} + \frac{n_{rmv}}{\lambda_{rmv}} + \lambda_{rpl} n_{rpl}\right], \quad 0 < \alpha_i, \lambda_{rmv}, \lambda_{rpl} \le 1 \tag{18}$$

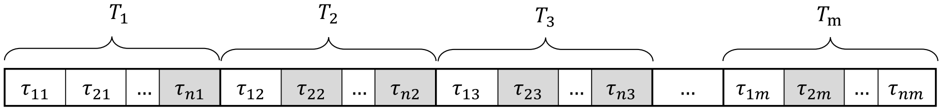

Fig. 6. Schematic chromosome structure containing tag placement options for a project with m phases [shaded (gray) genes indicate the infeasible tag placement option at each construction phase].

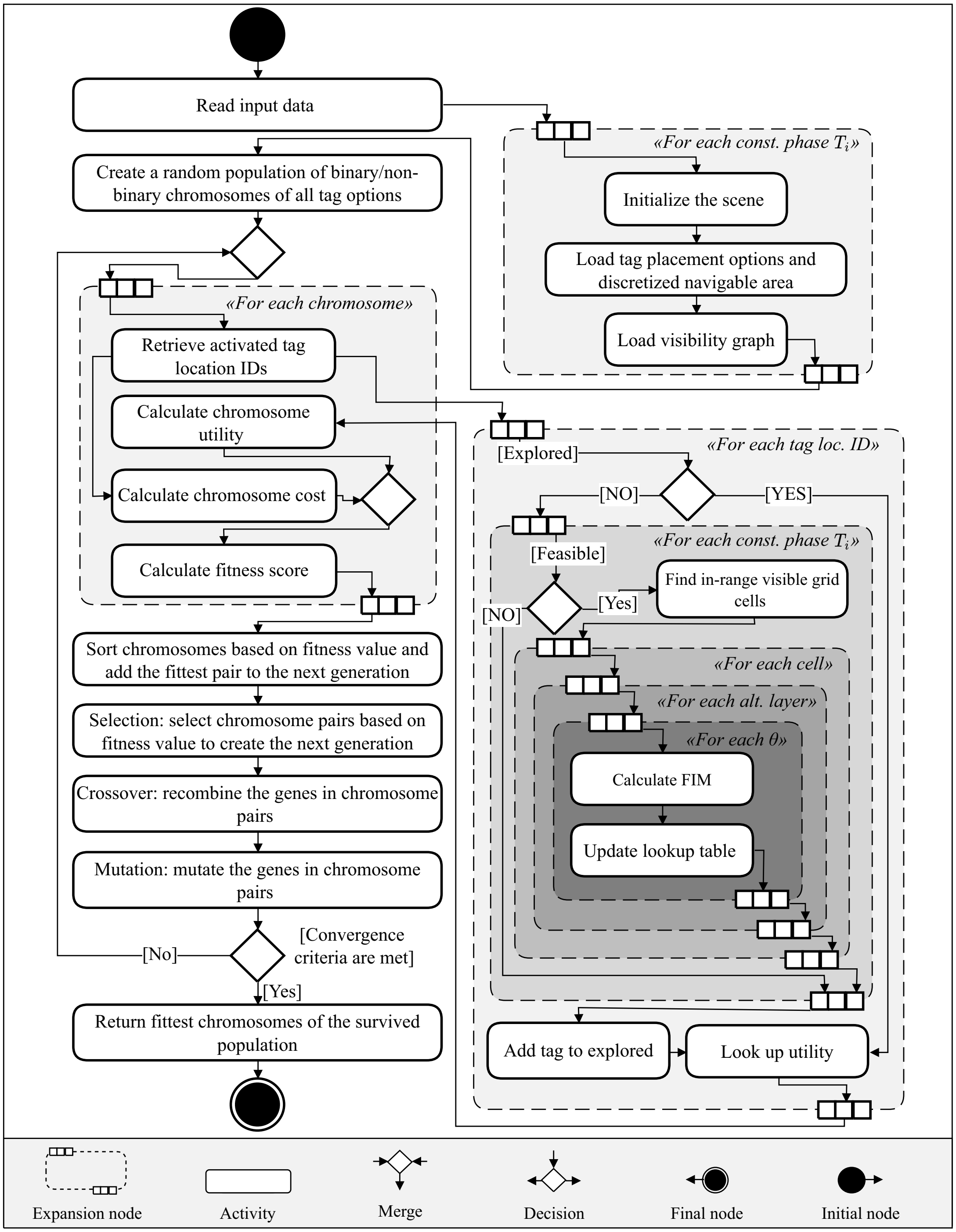
Read input data
Create a random population of binary/non-binary chromosomes of all tag options
«For each const. phase T_i»
Initialize the scene
Load tag placement options and discretized navigable area
Load visibility graph
«For each chromosome»
Retrieve activated tag location IDs
Calculate chromosome utility
Calculate chromosome cost
Calculate fitness score
«For each tag loc. ID»
[Explored]
[NO]
[YES]
«For each const. phase T_i»
[Feasible]
[Yes]
[NO]
Find in-range visible grid cells
«For each cell»
«For each alt. layer»
«For each θ»
Calculate FIM
Update lookup table
Add tag to explored
Look up utility
Sort chromosomes based on fitness value and add the fittest pair to the next generation
Selection: select chromosome pairs based on fitness value to create the next generation
Crossover: recombine the genes in chromosome pairs
Mutation: mutate the genes in chromosome pairs
[No]
[Convergence criteria are met]
[Yes]
Return fittest chromosomes of the survived population
Expansion node
Activity
Merge
Decision
Final node
Initial node

Fig. 7. UML activity diagram of GA engine.

$$w_{plc} = S_{\min} \times P_c \times n_{\text{cells}} \tag{19}$$

The cost function J penalizes adding extra tags to the network by expecting a minimum utility contribution. It also accounts for the sequential relation between construction phases by considering the entire project (i.e., chromosome) and penalizing the unnecessary changes in the tag network over time. The cost is a function of the number of placements (n_{plc}), replacements (n_{rpl}), and removals (n_{rmv}) throughout the entire project [Eq. (18)]. It assumes that tags need replacements every k phases (e.g., due to damages or being covered), and the number of available tag sizes is n_s. An accessibility coefficient ($0 < \alpha_i \leq 1$) is defined for each tag size to account for its practicality. The tag size with the unit accessibility coefficient is denoted as the project reference tag. The minimum utility contribution of a single reference tag is denoted as w_{plc}, while λ_{rmv} and λ_{rpl} represent the relative weights for tag removals and replacements, respectively. Thanks to the normalized gridwise utility calculations, w_{plc} can be specified as the minimum score ($S_{\min}$) that P_c percent of the cells are expected to gain [Eq. (19)].

As depicted in Fig. 7, GA-based optimization begins with reading input data, including tag placement options, navigable grid cells, and visibility graphs for senses in each construction phase. Then, a random population of chromosomes is generated for all tag placement options across all construction phases. Next, the activated tag location IDs for each chromosome (i.e., nonzero genes) are identified. The utility is directly looked up from the hash table if they are already explored. Otherwise, it explores the scenes of all construction phases to obtain the utilities while updating the table for later exploitations. The fitness score for each chromosome in the population is calculated by incorporating the cost. The fittest pair is found and added to the next generation by sorting the population by score. The next generation's population is created by performing selection, crossover, and mutation operations. The selection operator randomly selects a pair of chromosomes whose fitness values weigh the selection probability. The crossover switches segments of the genes in selected pairs to create a new offspring based on different techniques (e.g., one-point, two-point, and uniform). The mutation creates a minor random tweak in the offspring chromosomes (e.g., shuffling and flipping) to introduce diversity in the population. Finally, the fittest chromosomes are returned if the termination condition is met (e.g., the maximum number of iterations).

Validation

The proposed method was implemented in Python 3.8 with process-based parallelism. A sample model of a 64-m^2 unit in its early construction stages was chosen as an exploratory case. As depicted in Fig. 8, the project has three phases with identical ROIs. Moreover, a project of size 470 m^2 (Fig. 10) was incorporated to further investigate the proposed method's capability in handling large projects. The experiments were carried out in a BIM-enabled, photo-realistic simulation environment, enabling safe and efficient tests supported by absolute ground truth data. The simulation tool was developed on top of Parrot-Sphinx 1.2.1 (Parrot Drones SAS, Paris) and Gazebo, the open-source 3D robotics simulator in the robotic operating system (ROS) (Quigley et al. 2009). It was shown that the simulation experiments accurately mimic real-world experiments conducted in controlled laboratory environments (Kayhani et al. 2022). The platform used in the experiments was Parrot Bebop2, a compact, inexpensive UAV. This section addresses several questions. (1) How effectively does the proposed method maximize localizability and enhance robustness? (2) How do different metric functions perform? (3) How well can the proposed cost function avoid unnecessary changes in the 4D tag placement of a multiphase project? (4) What are some suggested values for the main parameters in PGA-TaPP? (5) How well does the method scale up to large projects?

Experiment Setup

Localizability Experiments

The root-mean-square error (RMSE) in 3D position estimates in different scenarios was compared to investigate the effectiveness of the proposed utility and candidate metric functions in maximizing localizability. The optimal configuration was found in each experiment based on a certain maximum number of tags and different metric functions, including FIM- and non-FIM-based. Based on previous observations (Kayhani et al. 2020), larger tags in the image often result in more accurate localization. To investigate this hypothesis, the area of the detectable tags in the image was incorporated as an alternative to the FIM to compute utility. A semirandom algorithm (denoted as *random*) was implemented as a baseline for comparison. The *random* algorithm generates 100 feasible tag configurations and returns the one with the highest score. Finally, the configuration in which all tag placement options are occupied determines the RMSE's lower bound for tag-based localization. Due to the limited camera FoV and line-of-sight, the measurements' quality and quantity depend on the vehicle's pose. Therefore, the RMSE may differ depending on the UAV's trajectory. Accordingly, we limited our investigations to three planar trajectories that are common maneuvers in automated indoor construction data collection: (1) Crab Walk (CWK); (2) Look Straight Ahead (LSA); and (3) Spinning (SPN) (Fig. 9).

The localizability experiments consider a scenario with a single phase, flight altitude, tag installation height, and tag size. In these experiments, the project's 3D BIM was imported into the simulation environment, where tag models were automatically generated and populated based on the 85 tag placement options identified in Modeling and Problem Formulation. The UAV autonomously followed the paths in Fig. 9, where the odometry and the camera feed were recorded for further analyses. The 3D position of the UAV was estimated using our tag-based localization, given the tag configuration obtained in each scenario. These tests concentrate on phase T_3 in Fig. 8, where the flight altitude and tag installation height were set to 1.5 m and only tags of size 23 × 23 cm were assumed to be available.

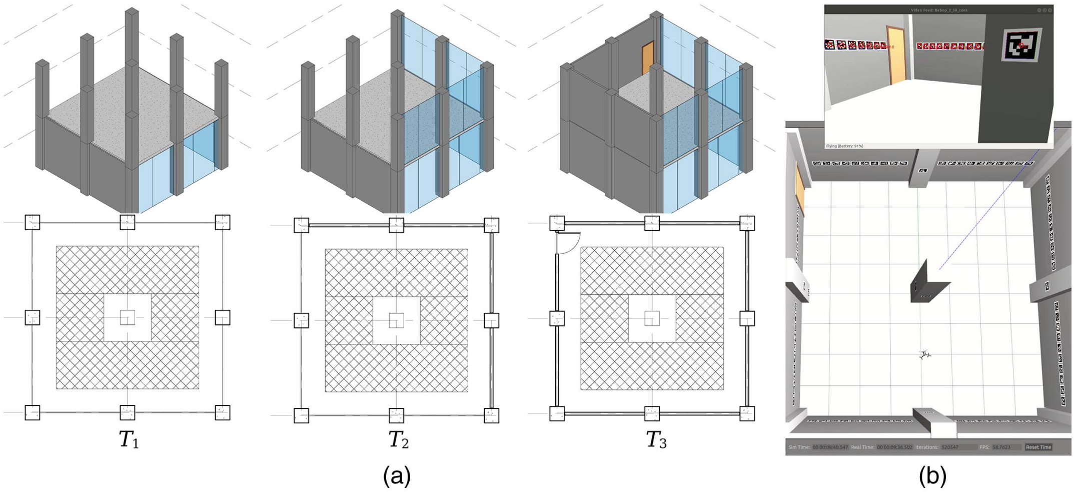

Fig. 8. (a) Sample project with three phases at top, and plan view with ROIs hashed and 3D models, bottom; and (b) UAV in the simulation environment, bottom, and its camera image stream with detected tags at top.

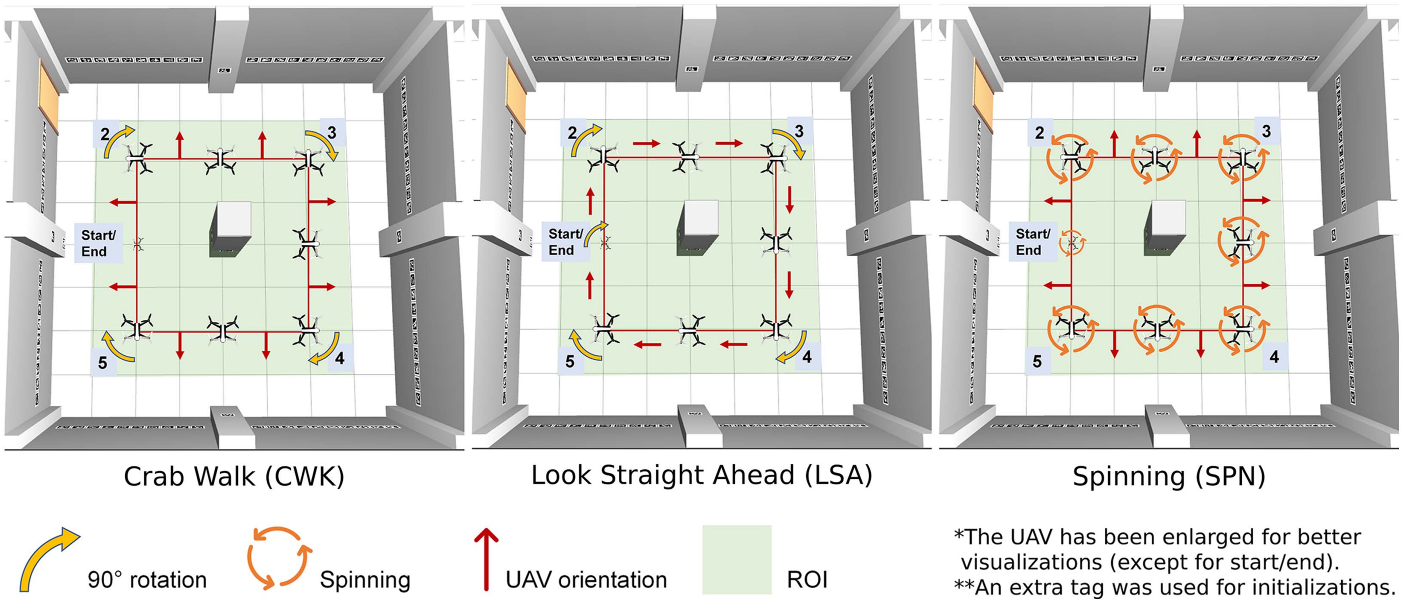

*The UAV has been enlarged for better visualizations (except for start/end).
**An extra tag was used for initializations.

Fig. 9. Threefold trajectories used in the localizability experiments.

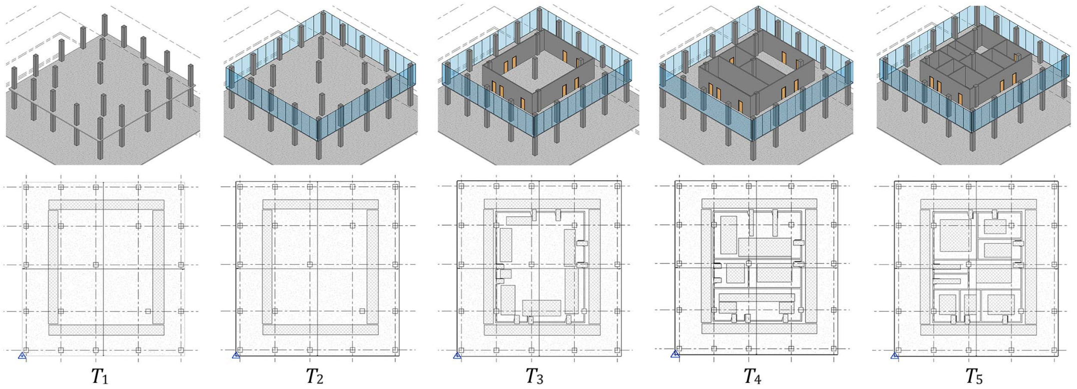

Fig. 10. A 470-m^2 project with five phases. ROIs (hashed polygons) change with construction progress.

Cost Function Experiments

An optimal 4D tag placement plan uses more practical tag sizes while providing maximum localizability with a minimum number of tags and tag configuration adjustments between phases. The installation costs are regularized by penalizing the deployment of less desirable tag sizes and changes in tag configuration between the project phases. The cost function experiments aim to study the effectiveness of our approach in reducing installation costs. To this end, the same multiphase project shown in Fig. 8 was used. Flight altitudes included 1.5 m and 2 m, the tag installation heights were 1 m and 1.5 m, and tags with side lengths of 23 cm, 16.5 cm, and 12.5 cm were assumed to be available. In these experiments, localizability utilities and the number of placements and removals were compared with and without the cost function incorporation. Unlike the localizability experiments, the maximum number of tags was 32. However, with the cost function incorporated, the optimal number of tags in each phase was found also based on the minimum tag score contribution, specified by w_{plc}.

Large Project Experiment

To evaluate the proposed method's performance in handling large projects, a 470-m^2 project with five phases was chosen (Fig. 10). The installation height and flight altitude were limited to 1.5 m. The maximum number of tags was 80, and tag sizes were limited to 16.5 cm, printable on letter-size sheets. In this scenario, ROIs and tag placement options change with construction progress. New locations may need to be visited by the UAV, and placement options might be created/removed for tag installation. Finally, the planning and GA parameters listed in Table 1 were kept unchanged across all experiments to make the results comparable.

Results

Localizability Experiments

Fig. 11 compares the localization accuracy for the optimal tag configurations in the threefold trajectories, grouped by metric functions and the maximum number of tags. Overall, by adding more tags, RMSE decreases as more measurements are received. Among the trajectories, SPN seems to be more challenging for our localization method, as it includes many rotational motions. Almost in all scenarios, the FIM-based utility outperforms the alternative metrics in terms of localization accuracy, among which trace had the lowest error in virtually all scenarios. Therefore,

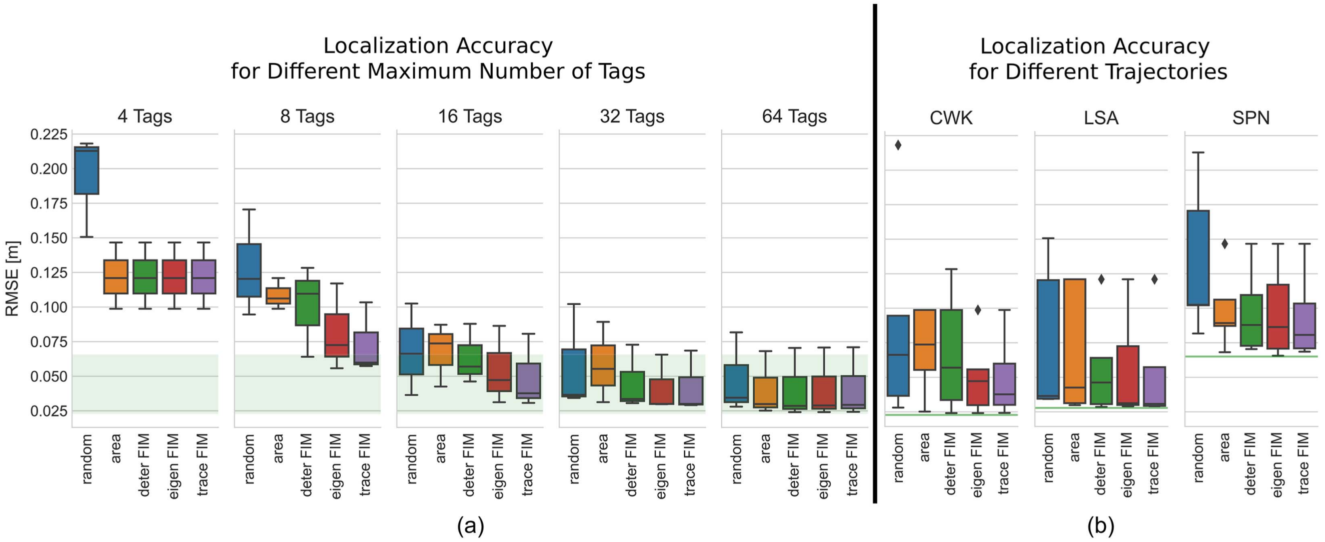

Fig. 11. RMSE in 3D position estimates for different metric functions in localizability experiments. The green range (a) and line (b) correspond to the RMSE's lower bound, where all tag placement options were occupied.

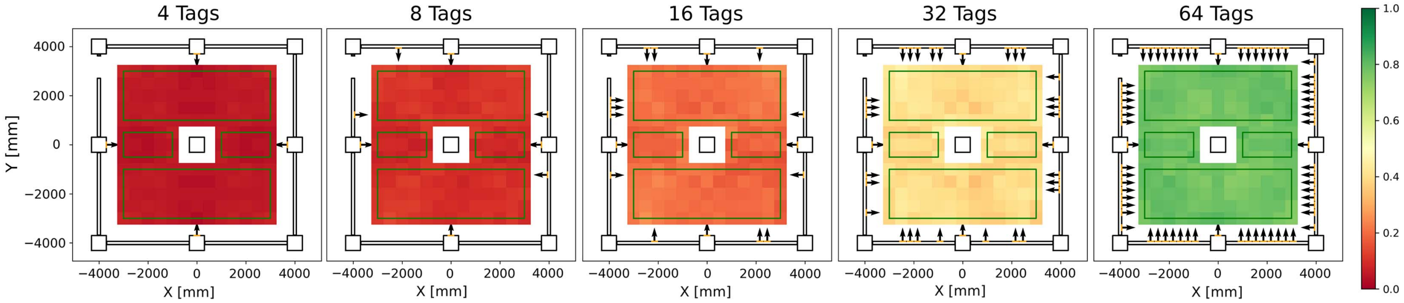

Fig. 12. Suggested tag configurations in localizability experiments using the FIM trace. The modified ROIs are displayed as four (green) boxes, and the normalized cell utilities are visualized as a heatmap.

we limit our discussions to the FIM trace as the metric function for the rest of this discussion. The optimal tag configurations found using the FIM trace are shown in Fig. 12, where the modified ROIs (compare with Fig. 9) are illustrated as boxes, and occupied tag placement options are shown as segment lines with an arrow symbol indicating their direction. The heatmap in Fig. 12 suggests the smooth distribution of the normalized grid utilities, where green cells are closer to their maximum attainable utility than yellow and red ones.

Cost Function Experiments. As shown in Fig. 13, the GA increases the fitness score with more iterations and successfully converges to a solution. Without the cost function, the algorithm finds the best tag locations for each phase separately. However, there is no mechanism except for the maximum number of tags to limit placing more tags per phase. The algorithm can choose between tag sizes based only on the utility. More importantly, as there is no notion of time and the relationship between the phases in the utility, the algorithm repeatedly changes the location and the size of the tags between phases. Without cost, 70 tags were used throughout the project. With cost function, on the other hand, PGA-TaPP optimizes the tag configuration by using 33 tags while mainly using the more practical reference tag (16.5 cm) and keeping the changes in the network at a minimum. The results and the input parameters are summarized in Table 2.

Large Project Experiment. The previous experiments qualitatively and quantitatively showed that PGA-TaPP could successfully maximize localizability via the utility function while minimizing the installation costs through the cost function. Although the limited tag placement options differed between the phases, the ROIs were assumed to be unchanged in the previous experiments. This experiment investigated the method's scalability by studying a more sophisticated scenario with almost 1,000 tag placement options across phases where ROIs update as the project progresses.

As seen in Fig. 14, the larger search space makes the convergence slower. However, given the input parameters in Table 2, PGA-TaPP provides a 4D plan with a minimal number of tag adjustments throughout the project. As shown in Figs. 14 and 15, the number of tags in T_1 and T_2 were 14 and 12, respectively, and less than 80. This is to limit the number of removals in the later phases. However, from T_3 on, the maximum number of tags was deployed. Fig. 15 illustrates the number of tags previously or newly added to the network in each phase.

Discussion

Localizability with a Minimum Number of Tags

To reduce the manual tag placement, the planner needs to maximize localizability with a minimum number of tags. The results in Fig. 11

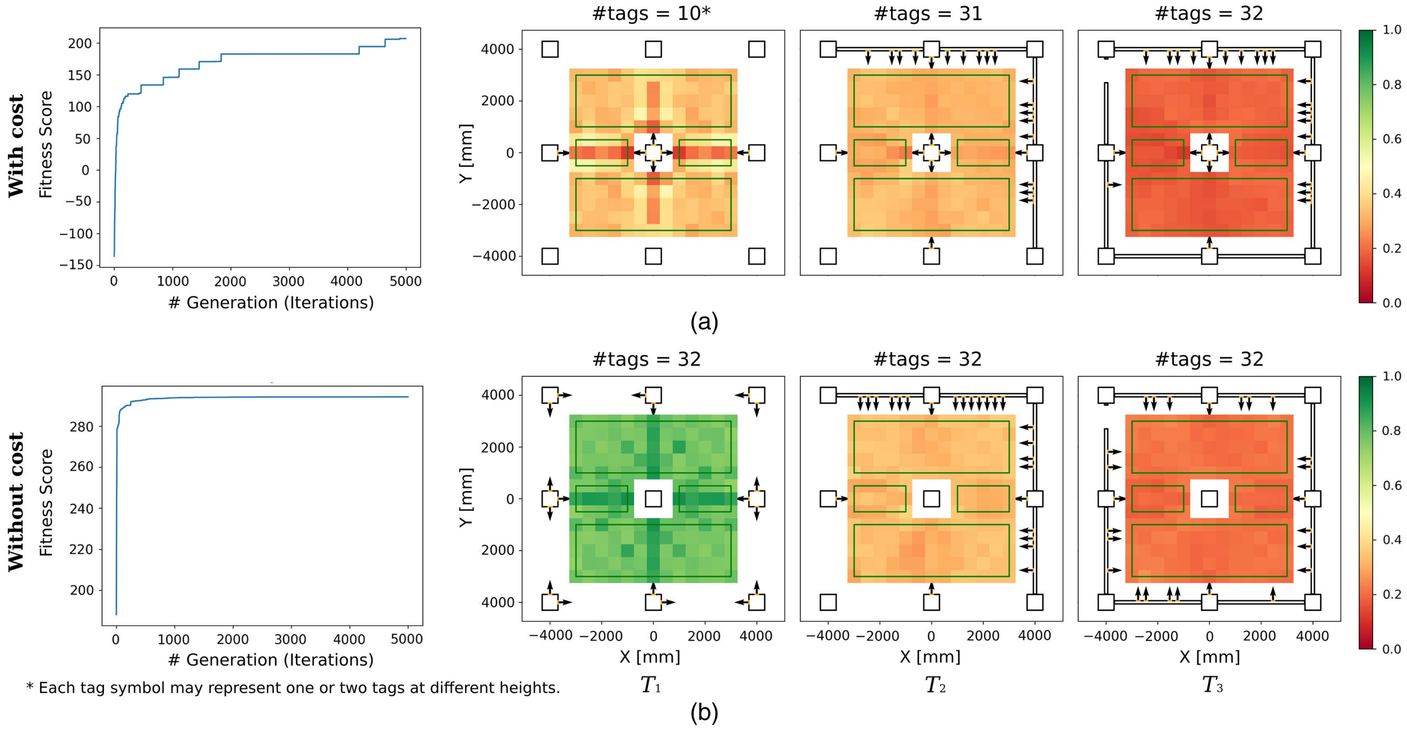

Fig. 13. Impact of cost function on penalizing tag configuration changes throughout the project: (a) fittest solution score in each iteration; and (b) optimal tag configurations in each phase. The first and last rows illustrate the results with and without cost function incorporation, respectively.

Table 2. Input parameters and the number of placement and removals in cost function and large project experiments

Parameters	Cost function experiments		Large project experiment
	With cost	Without cost	
	Inputs		
w_{plc}	$S_{\min} = 6\%$, $P_c = 2\%$	0	$S_{\min} = 1\%$, $P_c = 0.5\%$
Tag sizes (cm)	[12.0, 16.5, 23.0]	[12.0, 16.5, 23.0]	[16.5]
α_i	[0.5, 1.0, 0.5]	N/A	[1.0]
λ_{rmv}, λ_{rpl}	0.1, 0.0	N/A	1.0, 0.0
	Outputs		
n_{plc} (total)	[2, 26, 5] (33)	[21, 16, 33] (70)	[142] (142)
n_{rmv}	1	28	70

indicate that the FIM and the candidate metric functions effectively capture the notion of tag-based localizability, unlike area and the *random* algorithm. Above all, the trace FIM achieved the RMSE's lower bound—i.e., all tag placement options were occupied, using only 40% of the available options. This demonstrates that the proposed utility function effectively maximizes localizability and enhances robustness by smoothly distributing the utility across the grids. Additionally, the trace was shown to perform better than the other more computationally expensive FIM-based metric functions, which can also improve planning efficiency.

Construction Progress, Project Schedule, and Tag Size

The indoor layout changes with construction progress, requiring the planner to take the dynamic nature of construction into account and avoid any unnecessary tag network adjustments as the project progresses. To this end, the proposed method automatically extracts the indoor 2D layout at given times from the as-designed or updated 4D-BIM. Without a 4D-BIM, this information should be extracted manually. The results from cost function experiments (Fig. 13) suggest that, by incorporating the proposed cost function, PGA-TaPP considers the entire project to place tags with higher size desirability in locations that would contribute to the localizability in multiple phases. As summarized in Table 2, with cost function incorporation, 33 tags were used for the whole project, suggesting a 57% reduction in the number of tags without cost function incorporation. The results suggest that the cost function successfully minimized the tag network modification and installation expenses. The algorithm tends to keep the tags for multiple phases, which may result in using fewer tags in the earlier phases. Although this behavior can be modified using the input parameters, we observed that the suggested parameters summarized in Table 3 work well for most scenarios.

Scalability

A practical 4D tag placement planner must remain relevant in large-scale construction projects. The results in Fig. 14 qualitatively demonstrate the efficacy of the proposed method in handling large projects. The modification of the tag network was kept to a minimum, while the localizability was maximized, despite the change in ROIs and layout between phases. The heatmap visualization is

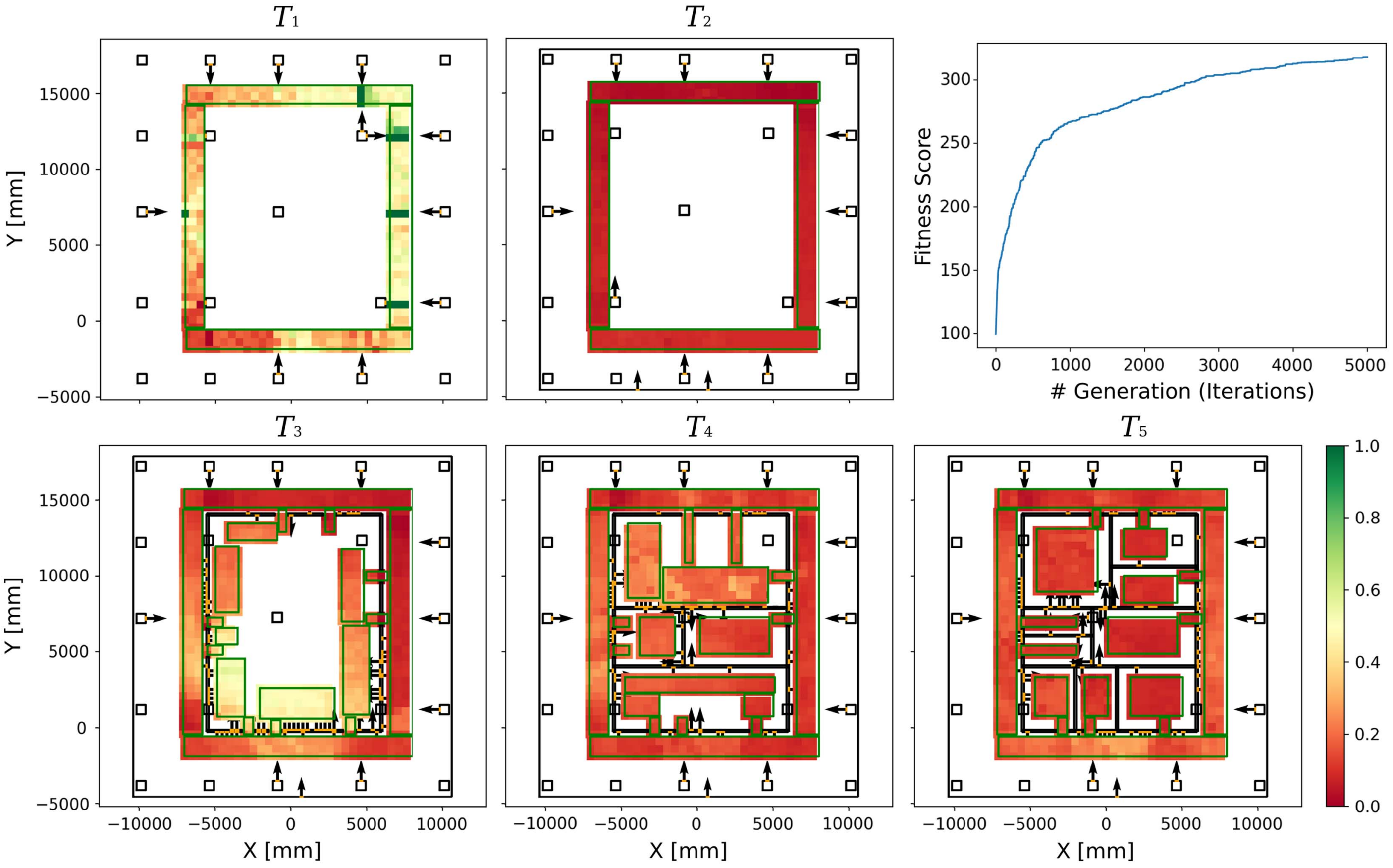

Fig. 14. 4D tag placement plan for the large project in which the ROIs and layout change over different phases.

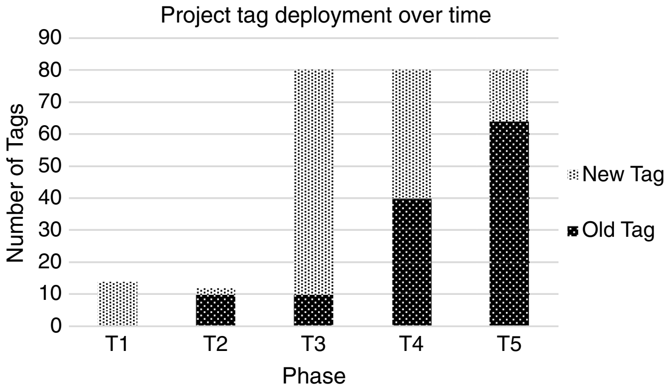

Fig. 15. Project tag deployment over time for large project experiment.

Table 3. PGA-TaPP parameters

Parameter	Value
ROI discretization resolution (m)	0.5
Rotation discretization step ($\Delta\theta$) (degrees)	20
Tag placement discretization resolution (m)	0.3
UAV's camera depth of view (DoV) (m)	8.0
ROIs' importance factor (I_{roi})	1.0
Population size	50
Maximum number of iterations	5,000
Mutation function	Flip
Crossover function	Single-point

based on the capacity utilization of each cell. In this case, the number of tag placement options increases with construction progress, while the maximum number of tags available is assumed to be 80. Therefore, the cell capacity increases more drastically than the utility gained, resulting in red cells. As shown in Fig. 15, PGA-TaPP plans the tag placement so that the tags from previous phases can be used in the next ones while maximizing the localizability with a limited number of tags. The total number of tags used was 14.8% of the total number of the options, which proves that the proposed method can effectively optimize the size, location, and number of tags to reduce the installation efforts and costs.

Conclusion

The tag-based visual-inertial method addresses some of the most important technical and practical localization challenges in indoor construction environments. These challenges include frequent layout changes, feature scarcity, and perceptual aliasing. However, tag placement and maintenance could be tedious if not properly planned. This study presented PGA-TaPP, a perception-aware genetic algorithm-based tag placement planner, to automatically identify the optimal tag configuration (i.e., size, location, number) and support tag-based visual-inertial indoor localization. This method maximizes localizability while minimizing tag installation costs by incorporating the project schedule and safety requirements. It considers multiple project phases, tag placement heights, flight altitudes, and metric functions. Localizability is quantified using the Fisher information matrix (FIM), and the installation cost is kept at a minimum by penalizing tag network modifications (e.g., adding extra tags). The effectiveness of our method was quantitively and qualitatively shown via three case studies. It was demonstrated that the proposed tag-based formulations for estimating the observed FIM represent localizability effectively. It was also experimentally demonstrated that the FIM trace could be a better metric function than determinants and the minimum eigenvalue. We showed that the maximum localizability was obtained using FIM-trace deploying only 40% of the available tag placement options in a single construction phase. In a sample multiphase project, the proposed cost function could reduce the number of deployed tags by 57% throughout the project. Finally, our experiments confirmed that the proposed method was scalable to larger projects, where the optimal number of tags was limited to 14.8% of the total number of options.

This work has some limitations. First, even though using metric functions can help compare FIMs, it cannot solely capture the spatial distribution of scores within and among ROIs. For example, the optimization algorithm may maximize the utility in scattered cells or isolated areas. Although robust localization is satisfied in these regions, reliable autonomous navigation will not necessarily be guaranteed between these isolated areas. These areas with locally concentrated high scores, denoted as islands, must be avoided. Although our experiments showed a relatively smooth distribution of scores, more studies are needed to comprehensively address this issue. A suggested alternative policy is to use a maximum threshold for each metric function to distribute the optimization attention and avoid islands. This threshold implies that we are no longer concerned with improving the localization quality once it reaches a certain level. Second, despite the intuitiveness and flexibility of evolutionary algorithms such as GA, they are local search techniques and do not guarantee global optimums. GA-based optimization can be slow in searching large spaces despite our efforts to parallelize processes. Accordingly, experimenting with other optimization techniques is highly recommended. Third, this work was validated in a simulation environment, mimicking controlled laboratory settings, as a proof of concept, while construction sites are dynamic and cluttered. A complementary study is needed to investigate the performance of the proposed method onsite during construction. Finally, other strategies for tag distribution, including surface spraying, using reflective plastic sheets (e.g., vinyl sheets) used in street signs, and horizontal tag placement (e.g., on the floor) should be studied. Other suggestions for future work include investigating the impact of onsite dynamic (e.g., workers) and temporary objects (e.g., formworks), dust, and lighting conditions on localizability.

Data Availability Statement

All data, models, or code that support the findings of this study are available from the corresponding author upon reasonable request.

Acknowledgments

The authors appreciate the financial support from the Natural Science and Engineering Research Council (NSERC) (Grant No. RGPIN-2017-06792). The opinions, findings, and conclusions presented in this work are those of the authors and do not necessarily reflect the views of the entity mentioned previously.

References

Adán, A., B. Quintana, S. A. Prieto, and F. Bosché. 2020. "An autonomous robotic platform for automatic extraction of detailed semantic models of buildings." *Autom. Constr.* 109 (Jan): 102963. https://doi.org/10.1016/j.autcon.2019.102963.

Asadi, K., A. Kalkunte Suresh, A. Ender, S. Gotad, S. Maniyar, S. Anand, M. Noghabaei, K. Han, E. Lobaton, and T. Wu. 2020. "An integrated UGV-UAV system for construction site data collection." *Autom. Constr.* 112 (Apr): 103068. https://doi.org/10.1016/j.autcon.2019.103068.

Barfoot, T. D. 2017. *State estimation for robotics*. Cambridge, UK: Cambridge University Press.

Brommer, C., D. Malyuta, D. Hentzen, and R. Brockers. 2018. "Long-duration autonomy for small rotorcraft UAS including recharging." In *Proc., 2018 IEEE/RSJ Int. Conf. on Intelligent Robots and Systems (IROS)*, 7252–7258. New York: IEEE.

Cadena, C., L. Carlone, H. Carrillo, Y. Latif, D. Scaramuzza, J. Neira, I. Reid, and J. J. Leonard. 2016. "Past, present, and future of simultaneous localization and mapping: Toward the robust-perception age." *IEEE Trans. Rob. Autom.* 32 (6): 1309–1332. https://doi.org/10.1109/TRO.2016.2624754.

Cai, S., Z. Ma, M. J. Skibniewski, and S. Bao. 2019. "Construction automation and robotics for high-rise buildings over the past decades: A comprehensive review." *Adv. Eng. Inf.* 42 (Oct): 100989. https://doi.org/10.1016/j.aei.2019.100989.

Deasy, T. P., and W. G. Scanlon. 2004. "Stepwise algorithms for improving the accuracy of both deterministic and probabilistic methods in WLAN-based indoor user localization." *Int. J. Wirel. Inf. Netw.* 11 (4): 207–216. https://doi.org/10.1007/s10776-004-1234-1.

Delmerico, J., and D. Scaramuzza. 2018. "A benchmark comparison of monocular visual-inertial odometry algorithms for flying robots." In *Proc., 2018 IEEE Int. Conf. on Robotics and Automation*, 2502–2509. New York: IEEE. https://doi.org/10.1109/ICRA.2018.8460664.

Freimuth, H., and M. König. 2018. "Planning and executing construction inspections with unmanned aerial vehicles." *Autom. Constr.* 96 (Dec): 540–553. https://doi.org/10.1016/j.autcon.2018.10.016.

Gheisari, M., J. Irizarry, and B. N. Walker. 2014. "UAS4SAFETY: The potential of unmanned aerial systems for construction safety applications." In *Proc., Construction Research Congress 2014*, 1801–1810. Reston, VA: ASCE.

Ham, Y., K. K. Han, J. J. Lin, and M. Golparvar-Fard. 2016. "Visual monitoring of civil infrastructure systems via camera-equipped unmanned Aerial vehicles (UAVs): A review of related works." *Visualization Eng.* 4 (1): 1. https://doi.org/10.1186/s40327-015-0029-z.

Hamledari, H., B. McCabe, and S. Davari. 2017. "Automated computer vision-based detection of components of under-construction indoor partitions." *Autom. Constr.* 74 (Feb): 78–94. https://doi.org/10.1016/j.autcon.2016.11.009.

Hamledari, H., S. Sajedi, B. McCabe, and M. Fischer. 2021. "Automation of inspection mission planning using 4D BIMs and in support of unmanned aerial vehicle-based data collection." *J. Constr. Eng. Manage.* 147 (3): 04020179. https://doi.org/10.1061/(ASCE)CO.1943-7862.0001995.

Ibrahim, A., A. Sabet, and M. Golparvar-Fard. 2019. "BIM-driven mission planning and navigation for automatic indoor construction progress detection using robotic ground platform." In Vol. 1 of *Proc., 2019 European Conf. for Computing in Construction*, 182–189. Sint-Niklaas, Belgium: European Council on Computing in Construction.

Ibrahim, M., and O. Moselhi. 2016. "Inertial measurement unit based indoor localization for construction applications." *Autom. Constr.* 71 (Part 1): 13–20. https://doi.org/10.1016/j.autcon.2016.05.006.

Jin, M., S. Liu, S. Schiavon, and C. Spanos. 2018. "Automated mobile sensing: Towards high-granularity agile indoor environmental quality monitoring." *Build. Environ.* 127 (Jan): 268–276. https://doi.org/10.1016/j.buildenv.2017.11.003.

Kayhani, N., A. Heins, W. Zhao, M. Nahangi, B. McCabe, and A. Schoellig. 2019. "Improved tag-based indoor localization of UAVs using extended kalman filter. In *Proc., 36th Int. Symp. on Automation and Robotics in Construction, ISARC 2019*, 624–631. Banff, AB, Canada: International Association for Automation and Robotics in Construction.

Kayhani, N., B. McCabe, A. Abdelaal, A. Heins, and A. P. Schoellig. 2020. "Tag-based indoor localization of UAVs in construction environments: Opportunities and challenges in practice." In *Proc., Construction Research Congress 2020*, 226–235. Reston, VA: ASCE.

Kayhani, N., W. Zhao, B. McCabe, and A. P. Schoellig. 2022. "Tag-based visual-inertial localization of unmanned aerial vehicles in indoor construction environments using an on-manifold extended Kalman filter." *Autom. Constr.* 135 (Mar): 104112. https://doi.org/10.1016/j.autcon.2021.104112.

Kielhauser, C., R. Renteria Manzano, J. J. Hoffman, and B. T. Adey. 2020. "Automated construction progress and quality monitoring for commercial buildings with unmanned aerial systems: An application study from Switzerland." *Infrastructures* 5 (11): 98. https://doi.org/10.3390/infrastructures5110098.

Kim, P., J. Chen, and Y. K. Cho. 2018. "SLAM-driven robotic mapping and registration of 3D point clouds." *Autom. Constr.* 89 (May): 38–48. https://doi.org/10.1016/j.autcon.2018.01.009.

Laakso, A. 2012. "The IFC standard: A review of history, development, and standardization, information technology." *ITcon* 17 (9): 134–161.

Lin, J. J., A. Ibrahim, S. Sarwade, and M. Golparvar-Fard. 2021. "Bridge inspection with aerial robots: Automating the entire pipeline of visual data capture, 3D mapping, defect detection, analysis, and reporting." *J. Comput. Civ. Eng.* 35 (2): 04020064. https://doi.org/10.1061/(ASCE)CP.1943-5487.0000954.

Liu, T., L. Yang, Q. Lin, Y. Guo, and Y. Liu. 2014. "Anchor-free backscatter positioning for RFID tags with high accuracy." In *Proc., IEEE INFOCOM*, 379–387. New York: IEEE. https://doi.org/10.1109/INFOCOM.2014.6847960.

Lozano-Pérez, T., and M. A. Wesley. 1979. "An algorithm for planning collision-free paths among polyhedral obstacles." *Commun. ACM* 22 (10): 560–570. https://doi.org/10.1145/359156.359164.

Mantha, B. R. K., C. C. Menassa, and V. R. Kamat. 2018. "Robotic data collection and simulation for evaluation of building retrofit performance." *Autom. Constr.* 92 (Aug): 88–102. https://doi.org/10.1016/j.autcon.2018.03.026.

Martinez, J. G., G. Albeaino, M. Gheisari, R. R. A. Issa, and L. F. Alarcón. 2021. "iSafeUAS: An unmanned aerial system for construction safety inspection." *Autom. Constr.* 125 (May): 103595. https://doi.org/10.1016/j.autcon.2021.103595.

Moselhi, O., H. Bardareh, and Z. Zhu. 2020. "Automated data acquisition in construction with remote sensing technologies." *Appl. Sci.* 10 (8): 2846. https://doi.org/10.3390/app10082846.

Muñoz-Salinas, R., M. J. Marín-Jimenez, and R. Medina-Carnicer. 2019. "SPM-SLAM: Simultaneous localization and mapping with squared planar markers." *Pattern Recognit.* 86 (Feb): 156–171. https://doi.org/10.1016/j.patcog.2018.09.003.

Muñoz-Salinas, R., and R. Medina-Carnicer. 2020. "UcoSLAM: Simultaneous localization and mapping by fusion of keypoints and squared planar markers." *Pattern Recognit.* 101 (May): 107193. https://doi.org/10.1016/j.patcog.2019.107193.

Mur-Artal, R., J. M. M. Montiel, and J. D. Tardos. 2015. "ORB-SLAM: A versatile and accurate monocular SLAM system." *IEEE Trans. Rob.* 31 (5): 1147–1163. https://doi.org/10.1109/TRO.2015.2463671.

Neunert, M., M. Bloesch, and J. Buchli. 2016. "An open source, fiducial based, visual-inertial motion capture system." In *Proc., 2016 19th Int. Conf. on Information Fusion (FUSION)*, 1523–1530. New York: IEEE.

Pal, A., and S. H. Hsieh. 2021. "Deep-learning-based visual data analytics for smart construction management." *Autom. Constr.* 131 (Nov): 103892. https://doi.org/10.1016/j.autcon.2021.103892.

Quigley, M., B. Gerkey, K. Conley, J. Faust, T. Foote, J. Leibs, E. Berger, R. Wheeler, and A. Ng. 2009. *ROS: An open-source robot operating system*. New York: IEEE.

Rakha, T., and A. Gorodetsky. 2018. "Review of unmanned aerial system (UAS) applications in the built environment: Towards automated building inspection procedures using drones." *Autom. Constr.* 93 (Sep): 252–264. https://doi.org/10.1016/j.autcon.2018.05.002.

Razavi, S. N., and O. Moselhi. 2012. "GPS-less indoor construction location sensing." *Autom. Constr.* 28 (Dec): 128–136. https://doi.org/10.1016/j.autcon.2012.05.015.

Siebert, S., and J. Teizer. 2014. "Mobile 3D mapping for surveying earthwork projects using an unmanned aerial vehicle (UAV) system." *Autom. Constr.* 41 (May): 1–14. https://doi.org/10.1016/j.autcon.2014.01.004.

Teizer, J. 2015. "Status quo and open challenges in vision-based sensing and tracking of temporary resources on infrastructure construction sites." *Adv. Eng. Inf.* 29 (2): 225–238. https://doi.org/10.1016/j.aei.2015.03.006.

Wang, J., and E. Olson. 2016. "AprilTag 2: Efficient and robust fiducial detection." In *Proc., IEEE Int. Conf. on Intelligent Robots and Systems*, 4193–4198. New York: IEEE.

Wang, Z., and G. Dissanayake. 2008. "Observability analysis of SLAM using Fisher information matrix." In *Proc., 2008 10th Int. Conf. on Control, Automation, Robotics and Vision, ICARCV 2008*, 1242–1247. New York: IEEE.

Witrisal, K., and P. Meissner. 2012. "Performance bounds for multipath-assisted indoor navigation and tracking (MINT)." In *Proc., IEEE Int. Conf. on Communications*, 4321–4325. New York: IEEE.

Xu, L., C. Feng, V. R. Kamat, and C. C. Menassa. 2019. "An occupancy grid mapping enhanced visual SLAM for real-time locating applications in indoor GPS-denied environments." *Autom. Constr.* 104 (Aug): 230–245. https://doi.org/10.1016/j.autcon.2019.04.011.

Xu, L., C. Feng, V. R. Kamat, and C. C. Menassa. 2020. "A scene-adaptive descriptor for visual SLAM-based locating applications in built environments." *Autom. Constr.* 112 (Apr): 103067. https://doi.org/10.1016/j.autcon.2019.103067.

Yi, S., S. Worrall, and E. Nebot. 2019. "Metrics for the evaluation of localisation robustness." In *Proc., 2019 IEEE Intelligent Vehicles Symp. (5)*, 1247–1253. New York: IEEE.

Zhang, Z., and D. Scaramuzza. 2019. "Beyond point clouds: Fisher information field for active visual localization." In *Proc., 2019 Int. Conf. on Robotics and Automation (ICRA)*, 5986–5992. New York: IEEE.